EDITED BY **FA-LONG LUO**

Digital Front-End in Wireless Communications and Broadcasting

Circuits and Signal Processing

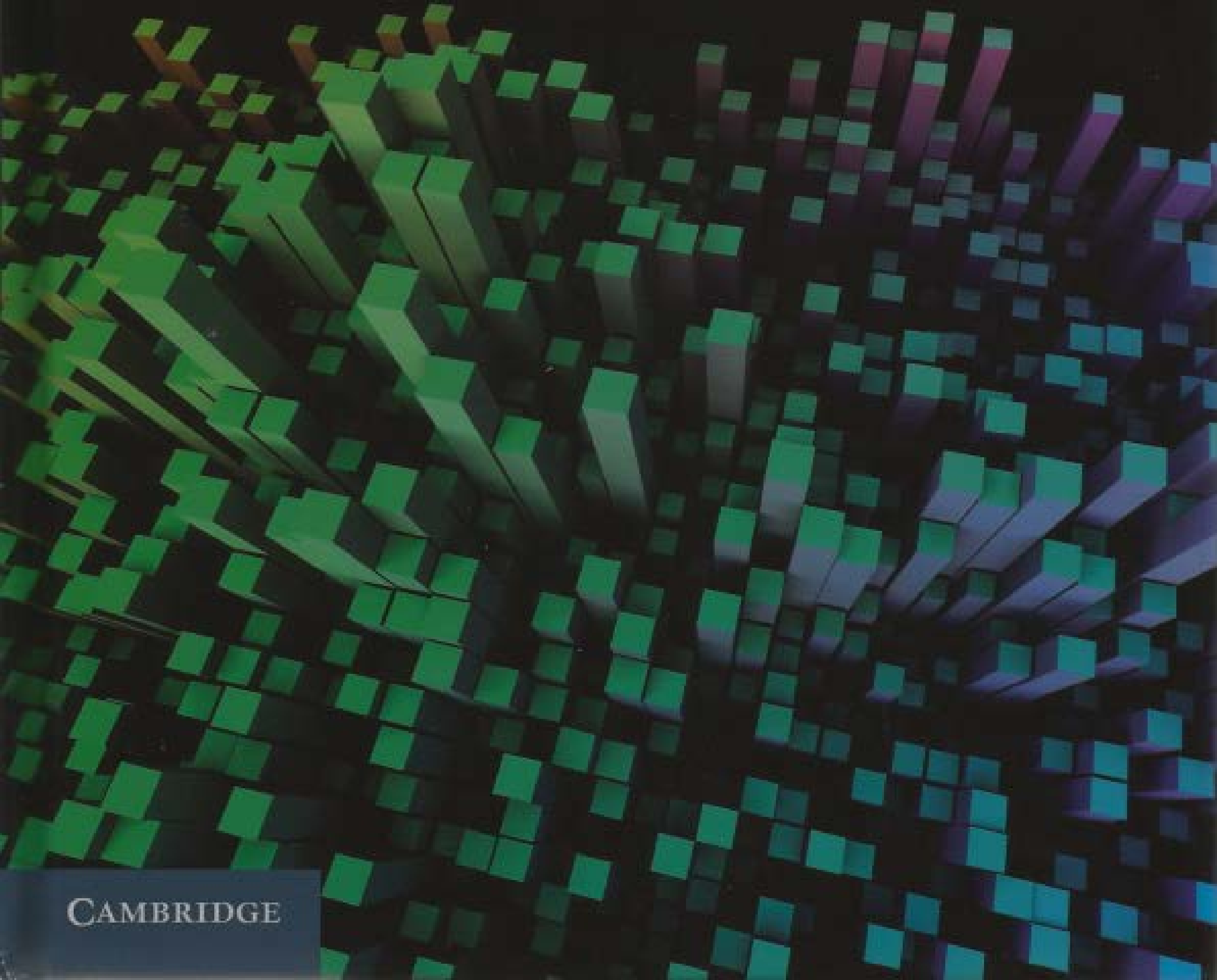

CAMBRIDGE

24 Multi-port front-end and transceivers for V-band multi-gigabit/s communication systems

Serioja Ovidiu Tatu, Emilia Moldovan, and Sofiene Affes

24.1 Introduction

The millimeter wave spectrum has been identified as a candidate of choice to support multi-gigabit/s data transmissions. The increasing interest of recent years has pushed the regulatory agencies to provide new opportunities for unlicensed spectrum usage with fewer restrictions on radio parameters. In order to provide more flexibility in spectrum sharing, the FCC introduced an opening of 7 GHz unlicensed spectrum at millimeter wave frequencies around 60 GHz, from 57 to 64 GHz.

As known, in the case of comparable bandwidths and data-rates, an important advantage of using millimeter wave frequencies instead of microwave ones is the reduced ratio between the bandwidth and the central frequency, leading the way to transceiver simplicity. In addition, compared to microwave frequencies, the strong signal attenuation at 60 GHz allows an efficient reuse. This helps to create small indoor cells for hot spot secure wireless communications. This spectrum is suitable for multi-gigabit/s wireless communication systems, which could be home or office high-speed wireless networking and entertainment, such as extremely fast downloading of files via wireless Gigabit Ethernet, and wireless High Definition Multimedia Interface (HDMI).

At the same time, the 60 GHz communication systems are also very attractive for secure line-of-sight multi-gigabit/s Low Earth Orbit inter-satellite links. The communications cannot be received on the Earth surface due to severe oxygen absorption in the atmosphere (around 20 dB/km at sea level). However, for this challenging application, major improvements must be made to today's emerging transceivers. There are still multiple challenges in terms of circuit and module design and fabrication, and system architectures. In the authors' opinion, the use of multi-port interferometric approach in conjunction with innovative fabrication technologies will open the way to low-cost reliable multi-gigabit/s millimeter wave communication systems. We are persuaded that the work presented in this chapter will lead the way to transceiver simplicity together with system miniaturization, ensuring higher data-rates, compared to the conventional microwave Ultra Wideband (UWB) approach. For example, a data-rate of 14 Gb/s is achievable using single carrier 16 symbols Quadrature Amplitude Modulation (16 QAM)

Digital Front-End in Wireless Communications and Broadcasting, ed. Fa-Long Luo. Published by Cambridge University Press.

or Orthogonal Frequency Division Multiplexing (OFDM) scheme with seven Quadrature Phase Shift Keying (QPSK) modulated carriers.

The multi-port circuit theory was first developed in the 1970s by scientists for accurate automated measurements of the complex reflection coefficient in microwave network analysis. These multi-port pioneers highlighted its usefulness in microwave low-cost circuit characterizations (S-parameters). Since 1994, the multi-port techniques were further developed by Professors R. G. Bosisio and Ke Wu (Poly-Grames Research Centre of "École Polytechnique de Montreal," Canada) and collaborators, who proposed its use as a microwave and millimeter wave demodulator in connection with homodyne and heterodyne receivers. Several multi-port architectures for specific applications have been developed and implemented. Basically, this is a passive circuit, composed of several couplers, interconnected by transmission lines and phase shifters. The multi-port acts as an interferometer; its output signals are linear combinations of phase shifted reference and input unknown signals. By using appropriate devices connected to output ports, this circuit can provide quadrature down-conversion or direct modulation.

Section 24.2 presents the multi-port interferometer theory focused on quadrature down-conversion, direct modulation of a millimeter wave signal, and antenna array implementation. This describes and analyzes various multi-port circuit implementations and their advantages versus the conventional approaches.

Section 24.3 deals with practical implementation, modeling, and analysis of a 60 GHz multi-port. Taking advantage of the advancements in fabrication technologies at microwave and millimeter wave frequencies, bulky waveguide circuits are integrated into various substrate integrated circuits (SICs). Multi-port circuit schemes and practical realizations using Miniature Hybrid Microwave Integrated Circuit (MHMIC) technology are presented and discussed. Despite its physical limitations, the conventional Rectangular Waveguide (RWG) technology is still essential to connect the SICs to standard millimeter wave equipment and circuits.

Section 24.4 proposes multi-port interferometric V-band transceiver architectures for wireless local area networks (WLANs), dedicated to high data-rate communications, including digital signal processing considerations. The use of a multi-port interferometer in quadrature down-conversion is an innovative approach, due to its intrinsic properties, such as wide bandwidth, reduced local oscillator (LO) power requirement, excellent isolation between RF input ports, and very good suppression of harmonic and spurious products. In addition, millimeter wave direct modulators and array antennas (implemented using multi-ports, as presented in Section 24.2), are considered in the proposed system architectures.

Advanced system simulation results, based on realistic circuit models, are presented and discussed in detail in Section 24.5, followed by conclusions in Section 24.6.

Computed aided design (CAD) tools, such as Advanced Design Systems (ADS) of Agilent Technologies and High Frequency Structure Simulator (HFSS) of Ansoft have been used for circuit designs and system simulations. Circuit prototype photographs, along with simulation and measurement results reinforce this presentation.

24.2 Multi-port interferometer theory

The multi-port, in fact a "six-port" circuit, was first developed by Cohn and Weinhouse [1] to evaluate the phase of a microwave signal, and extended by Engen and Hoer [2]–[4] for accurate automated measurements of the complex reflection coefficient in microwave network analysis.

Between 1972 and 1994, similar researches were pursued by other laboratories, including Poly-Grames Research Centre of "École Polytechnique de Montreal." The proposed six-port is a passive circuit, composed of hybrid couplers and/or power dividers, connected by transmission lines. It has two inputs, one for the unknown signal and the other for the reference signal, and four outputs. The output signals represent linear combinations of the input signals. The evaluation of the reflection coefficient is based on the measurement of output signal power levels. Detailed discussion is presented in [5].

In 1994, the idea of a multi-port circuit to be used in direct conversion microwave receivers was proposed for the first time at the Poly-Grames Research Centre of "École Polytechnique de Montreal." The first reported results were related to the narrow-band single-carrier demodulation of digital data [6]–[8]. The multi-port architecture was very similar to the original approach, and a calibration process was needed to perform measurements. Since 2001, various multi-port interferometer techniques with no need of calibration have been developed [9]–[12].

24.2.1 Multi-port interferometer for quadrature down-conversion

The multi-port circuit presented in Figure 24.1 is composed of three 90° hybrid couplers and a Wilkinson power divider. This architecture is typical for a multi-port microstrip implementation. The instantaneous phase shift and the relative amplitude between RF unknown and reference input signals, a_6 and a_5, respectively, are obtained by output power measurements, as explained below.

Generally, for a multi-port, the output signals, b_i, can be expressed as a function of the dispersion parameters S_{ij}:

$$b_i = \sum_{j=1}^{6} S_{ij} a_j, \quad i = 1, \ldots, 6 \tag{24.1}$$

The scattering matrix of the proposed multi-port phase discriminator can be obtained using the diagram presented in Figure 24.1. For this purpose, the following scattering matrices of a 90° hybrid coupler and Wilkinson power divider, as given in Equations (24.2) and (24.3), respectively, are used:

$$[S] = \frac{1}{\sqrt{2}} \begin{bmatrix} 0 & j & 1 & 0 \\ j & 0 & 0 & 1 \\ 1 & 0 & 0 & j \\ 0 & 1 & j & 0 \end{bmatrix}, \tag{24.2}$$

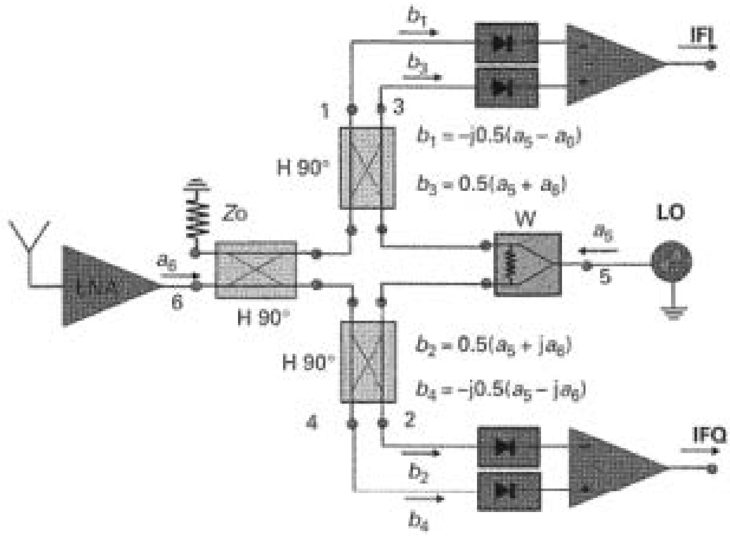

Figure 24.1 The multi-port interferometer for down-conversion in a front-end block diagram.

$$[S] = -j\frac{1}{\sqrt{2}}\begin{bmatrix} 0 & 1 & 1 \\ 1 & 0 & 0 \\ 1 & 0 & 0 \end{bmatrix}. \tag{24.3}$$

Therefore, according to Figure 24.1, the multi-port scattering matrix is obtained:

$$[S] = \frac{1}{2}\begin{bmatrix} 0 & 0 & 0 & 0 & -j & j \\ 0 & 0 & 0 & 0 & 1 & j \\ 0 & 0 & 0 & 0 & 1 & 1 \\ 0 & 0 & 0 & 0 & -j & -1 \\ -j & 1 & 1 & -j & 0 & 0 \\ j & j & 1 & -1 & 0 & 0 \end{bmatrix}. \tag{24.4}$$

The two normalized input waves having an α amplitude ratio, a $\Delta\varphi\,(t) = \varphi_6(t) - \varphi_5$ phase difference, and a $\Delta\omega = \omega - \omega_0$ frequency shift, can be expressed as follows:

$$a_5 = a \cdot e^{j(\omega_0 \cdot t + \varphi_5)}, \tag{24.5}$$

$$a_6 = \alpha \cdot a \cdot e^{j(\omega \cdot t + \varphi_6(t))} = \alpha \cdot a_5 \cdot e^{j(\Delta\omega \cdot t + \Delta\varphi(t))}. \tag{24.6}$$

Supposing a perfect match ($a_1 = a_2 = a_3 = a_4 = 0$), the four normalized output waves can be expressed depending on the input waves and related scattering (S) parameters:

$$b_i = a_5 \cdot S_{5i} + a_6 \cdot S_{6i}, \quad i = 1, \ldots, 4 \tag{24.7}$$

$$|b_i| = \frac{a}{2} \cdot \left|1 + \alpha \cdot e^{j\left[\Delta\omega \cdot t + \Delta\varphi(t) + (3-i)\frac{\pi}{2}\right]}\right|, \quad i = 1, \ldots, 4. \tag{24.8}$$

In order to obtain the IF output signals, four power detectors are connected to the multi-port outputs. As known, the output voltage of an ideal power detector is proportional to the square magnitude of the RF input signal:

$$v_i = K_i \cdot |b_i|^2 = K_i \cdot b_i \cdot b_i^*, \quad i = 1, \ldots, 4. \tag{24.9}$$

Supposing that identical power detectors are used, $K_i = K$, the output voltages become:

$$v_{1,3}(t) = K\frac{a^2}{4} \cdot \left\{1 + \alpha^2 \mp 2 \cdot \alpha \cdot \cos[\Delta\omega \cdot t + \Delta\varphi(t)]\right\}, \tag{24.10}$$

$$v_{2,4}(t) = K\frac{a^2}{4} \cdot \left\{1 + \alpha^2 \mp 2 \cdot \alpha \cdot \sin[\Delta\omega \cdot t + \Delta\varphi(t)]\right\}. \tag{24.11}$$

As seen, the output voltages at the pairs of ports 1 and 3, and 2 and 4, respectively, are phase opposites. Therefore, the quadrature output signals can be obtained using two differential amplifiers in the IF stage:

$$v_{IF}^I(t) = A_{IF} \cdot [v_3(t) - v_1(t)] = \alpha \cdot K \cdot a^2 \cdot A_{IF} \cdot \cos[\Delta\omega \cdot t + \Delta\varphi(t)], \tag{24.12}$$

$$v_{IF}^Q(t) = A_{IF} \cdot [v_4(t) - v_2(t)] = \alpha \cdot K \cdot a^2 \cdot A_{IF} \cdot \sin[\Delta\omega \cdot t + \Delta\varphi(t)]. \tag{24.13}$$

Finally, after the second frequency conversion and low-pass filtering, the baseband quadrature signals are obtained as follows:

$$I(t) = \frac{1}{2} \cdot \alpha \cdot a^2 \cdot K \cdot A_{IF} \cdot A_{BB} \cdot \cos[\Delta\varphi(t)], \tag{24.14}$$

$$Q(t) = \frac{1}{2} \cdot \alpha \cdot a^2 \cdot K \cdot A_{IF} \cdot A_{BB} \cdot \sin[\Delta\varphi(t)]. \tag{24.15}$$

Therefore, a baseband signal $\Gamma(t)$ can be defined in the complex plane:

$$\Gamma(t) = I(t) + jQ(t) = \frac{1}{2} \cdot \alpha \cdot a^2 \cdot K \cdot A_{IF} \cdot A_{BB} \cdot e^{j\Delta\varphi(t)}. \tag{24.16}$$

In order to highlight the differences versus the previous approach, the conventional quadrature mixer and a quasi-conventional multi-port proposal using anti-parallel diodes are presented in Figure 24.2.

The signal flow is calculated considering the scattering matrix of a Wilkinson divider, as presented in Equation (24.3), and the scattering matrix of a 180° hybrid coupler given by:

$$[S] = \frac{j}{\sqrt{2}} \begin{bmatrix} 0 & 1 & 1 & 0 \\ 1 & 0 & 0 & 1 \\ 1 & 0 & 0 & -1 \\ 0 & 1 & -1 & 0 \end{bmatrix}. \tag{24.17}$$

Therefore, the multi-port scattering matrix becomes:

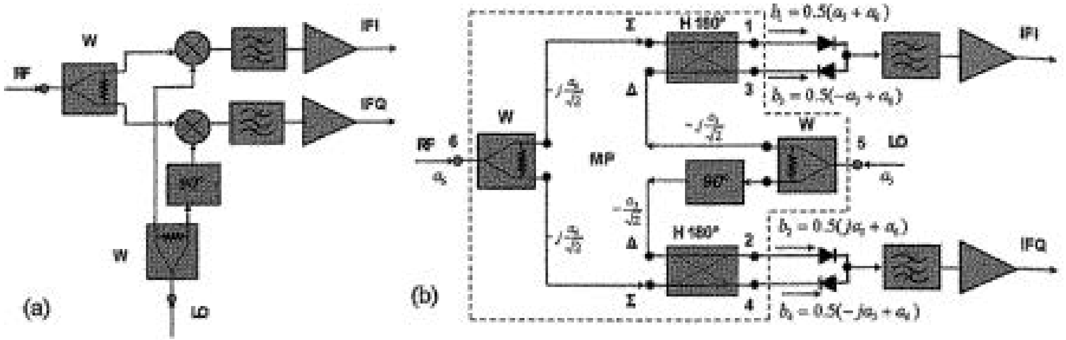

Figure 24.2 Block diagram of a conventional IQ mixer (a) and a quasi-conventional multi-port mixer (b).

$$[S] = \frac{1}{2}\begin{bmatrix} 0 & 0 & 0 & 0 & 1 & 1 \\ 0 & 0 & 0 & 0 & j & 1 \\ 0 & 0 & 0 & 0 & -1 & 1 \\ 0 & 0 & 0 & 0 & -j & 1 \\ 1 & j & -1 & -j & 0 & 0 \\ 1 & 1 & 1 & 1 & 0 & 0 \end{bmatrix}. \tag{24.18}$$

The 180° hybrid coupler output signals are injected into the anti-parallel diode inputs. Considering four identical diodes, and their general nonlinear characteristic:

$$I = c \cdot V + d \cdot V^2 + e \cdot V^3 + f \cdot V^4 + \cdots, \tag{24.19}$$

the in-phase current, before filtering, can be expressed as:

$$I^I = c \cdot (V_1 + V_3) + d \cdot \left(V_1^2 - V_3^2\right) + e \cdot \left(V_1^3 + V_3^3\right) + f \cdot \left(V_1^4 - V_3^4\right) + \cdots \tag{24.20}$$

$$I^I = c \cdot \sqrt{Z_0} \cdot (b_1 + b_3) + d \cdot Z_0 \cdot \left(b_1^2 - b_3^2\right) + e \cdot Z_0 \cdot \sqrt{Z_0} \cdot \left(b_1^3 + b_3^3\right) + f \cdot Z_0^2 \cdot \left(b_1^4 - b_3^4\right) + \cdots \tag{24.21}$$

Based on the calculus of b_i (see Equation (24.7)), as specified in Figure 24.2, after the required intermodulation product filtering, the only selected term is:

$$I_{IF}^I = -d \cdot Z_0 \cdot a_5 \cdot a_6. \tag{24.22}$$

In the same way, the related quadratic signal, after filtering, can be computed:

$$I_{IF}^Q = j \cdot d \cdot Z_0 \cdot a_5 \cdot a_6. \tag{24.23}$$

For down-conversion purposes, only the frequency difference term is selected after filtering.

We note that a main difference between the two down-conversion approaches exists. In the first implementation, the diodes are optimized to operate as power detectors. The output spectrum contains basically only low IF and DC signals. In the second one, due to the use of the whole nonlinear characteristic of diodes, the output spectrum is richer and must be carefully filtered. Therefore, in order to obtain comparable down-conversion results, the LO power must be considerably increased (with more than 20 dB) if the conventional approach is used [13].

24.2.2 Multi-port interferometer for direct modulation

The millimeter wave modulator is an essential element for the transmitter. Depending on the specific modulation scheme, a multi-port modulator or a millimeter wave switching network are proposed for low-cost UWB applications [14].

The multi-port modulator uses the multi-port interferometer presented in Figure 24.1, together with two pairs of mono-ports, having adjustable reflection coefficients. As seen in Figure 24.3, the normalized wave signal passing through the upper or lower hybrid coupler is multiplied by $j \cdot \Gamma_i$, $i = 1, 2$. The output signal of the direct modulator combines these signals as follow:

$$b_5 = 0.5 \cdot (\Gamma_1 + j\Gamma_2) \cdot a_6. \tag{24.24}$$

Therefore, the phase and the amplitude of the normalized output signal are related to the mono-port return loss values. The direct modulation of a millimeter wave signal is straightforward; the modulated constellation can be rotated in the IQ plane adding a constant phase shift.

As a first example using short or open circuits, the return loss values ($\Gamma_{1,2}$) are equal to -1 and $+1$, respectively, and conform to the direct modulation chart presented in Table 24.1; consequently, a direct QPSK multi-port modulator is obtained [14].

Different other modulated signals can be obtained using only the real part impedances for both mono-ports, as illustrated in Tables 24.2 to 24.4.

As detailed in the previous analysis, in order to obtain all modulation states, the ratio of the mono-port resistance maximum/minimum values (excepting open and short circuits, that are easily implemented with stubs) is equal to $7^2 = 49$ for Square

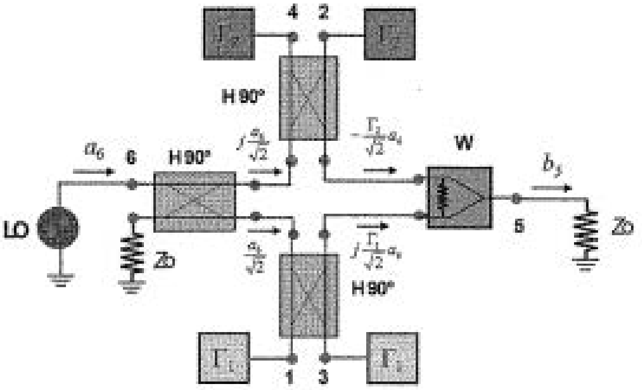

Figure 24.3 Simplified block diagram of multi-port direct modulator.

Table 24.1 QPSK direct modulation chart.

symbols	Gray code	Γ_1	Γ_2	$\boldsymbol{Z}_1$	$\boldsymbol{Z}_2$	$\boldsymbol{b}_5$
1	00	1	1	Open	Open	$0.5 \cdot (1+j) \cdot a_6$
2	01	-1	1	Short	Open	$0.5 \cdot (-1+j) \cdot a_6$
3	11	-1	-1	Short	Short	$0.5 \cdot (-1-j) \cdot a_6$
4	10	1	-1	Open	Short	$0.5 \cdot (1-j) \cdot a_6$

Table 24.2 8PSK direct modulation chart.

symbols	Gray code	Γ_1	Γ_2	$\boldsymbol{Z}_1$	$\boldsymbol{Z}_2$	$\boldsymbol{b}_5$
1	000	1	0	Open	Z_0	$0.5 \cdot a_6$
2	001	$\frac{1}{\sqrt{2}}$	$\frac{1}{\sqrt{2}}$	$\frac{\sqrt{2}+1}{\sqrt{2}-1} \cdot Z_0$	$\frac{\sqrt{2}+1}{\sqrt{2}-1} \cdot Z_0$	$\frac{0.5}{\sqrt{2}} \cdot (1+j) \cdot a_6$
3	011	0	1	Z_0	Open	$0.5 \cdot j \cdot a_6$
4	010	$-\frac{1}{\sqrt{2}}$	$\frac{1}{\sqrt{2}}$	$\frac{\sqrt{2}-1}{\sqrt{2}+1} \cdot Z_0$	$\frac{\sqrt{2}+1}{\sqrt{2}-1} \cdot Z_0$	$\frac{0.5}{\sqrt{2}} \cdot (-1+j) \cdot a_6$
5	110	-1	0	Short	Z_0	$-0.5 \cdot a_6$
6	111	$-\frac{1}{\sqrt{2}}$	$-\frac{1}{\sqrt{2}}$	$\frac{\sqrt{2}-1}{\sqrt{2}+1} \cdot Z_0$	$\frac{\sqrt{2}-1}{\sqrt{2}+1} \cdot Z_0$	$\frac{0.5}{\sqrt{2}} \cdot (-1-j) \cdot a_6$
7	101	0	-1	Z_0	Short	$-0.5 \cdot j \cdot a_6$
8	100	$\frac{1}{\sqrt{2}}$	$-\frac{1}{\sqrt{2}}$	$\frac{\sqrt{2}+1}{\sqrt{2}-1} \cdot Z_0$	$\frac{\sqrt{2}-1}{\sqrt{2}+1} \cdot Z_0$	$\frac{0.5}{\sqrt{2}} \cdot (1-j) \cdot a_6$

Table 24.3 Square 16-QAM direct modulation chart.

symbols	Gray code	Γ_1	Γ_2	$\boldsymbol{Z}_1$	$\boldsymbol{Z}_2$	$\boldsymbol{b}_5$
1	1000	0.75	-0.75	$7 \cdot Z_0$	$1/7 \cdot Z_0$	$(0.375 - j \cdot 0.375) \cdot a_6$
2	1001	0.75	-0.25	$7 \cdot Z_0$	$3/5 \cdot Z_0$	$(0.375 - j \cdot 0.125) \cdot a_6$
3	1011	0.75	0.25	$7 \cdot Z_0$	$5/3 \cdot Z_0$	$(0.375 + j \cdot 0.125) \cdot a_6$
4	1010	0.75	0.75	$7 \cdot Z_0$	$7 \cdot Z_0$	$(0.375 + j \cdot 0.375) \cdot a_6$
5	1110	0.25	0.75	$5/3 \cdot Z_0$	$7 \cdot Z_0$	$(0.125 + j \cdot 0.375) \cdot a_6$
6	1111	0.25	0.25	$5/3 \cdot Z_0$	$5/3 \cdot Z_0$	$(0.125 + j \cdot 0.125) \cdot a_6$
7	1101	0.25	-0.25	$5/3 \cdot Z_0$	$3/5 \cdot Z_0$	$(0.125 - j \cdot 0.125) \cdot a_6$
8	1100	0.25	-0.75	$5/3 \cdot Z_0$	$1/7 \cdot Z_0$	$(0.125 - j \cdot 0.375) \cdot a_6$
9	0100	-0.25	-0.75	$3/5 \cdot Z_0$	$1/7 \cdot Z_0$	$(-0.125 - j \cdot 0.375) \cdot a_6$
10	0101	-0.25	-0.25	$3/5 \cdot Z_0$	$3/5 \cdot Z_0$	$(-0.125 - j \cdot 0.125) \cdot a_6$
11	0111	-0.25	0.25	$3/5 \cdot Z_0$	$5/3 \cdot Z_0$	$(-0.125 + j \cdot 0.125) \cdot a_6$
12	0110	-0.25	0.75	$3/5 \cdot Z_0$	$7 \cdot Z_0$	$(-0.125 + j \cdot 0.375) \cdot a_6$
13	0010	-0.75	0.75	$1/7 \cdot Z_0$	$7 \cdot Z_0$	$(-0.375 + j \cdot 0.375) \cdot a_6$
14	0011	-0.75	0.25	$1/7 \cdot Z_0$	$5/3 \cdot Z_0$	$(-0.375 + j \cdot 0.125) \cdot a_6$
15	0001	-0.75	-0.25	$1/7 \cdot Z_0$	$3/5 \cdot Z_0$	$(-0.375 - j \cdot 0.125) \cdot a_6$
16	0000	-0.75	-0.75	$1/7 \cdot Z_0$	$1/7 \cdot Z_0$	$(-0.375 - j \cdot 0.375) \cdot a_6$

16-QAM, and $\left(\frac{\sqrt{2}+1}{\sqrt{2}-1}\right)^2 \approx 34$ for 8PSK and 16-Star QAM. Therefore, QPSK, 8PSK, and Star modulations are easier to implement. It is to be noted that, for demodulation purposes, the same modulations are less sensitive to both amplitude and phase noise.

Table 24.4 16-Star QAM direct modulation chart.

symbols	Gray code	Γ_1	Γ_2	Z_1	Z_2	b_5
1	0000	1	0	Open	Z_0	$0.5 \cdot a_6$
2	0001	$\frac{1}{\sqrt{2}}$	$\frac{1}{\sqrt{2}}$	$\frac{\sqrt{2}+1}{\sqrt{2}-1} \cdot Z_0$	$\frac{\sqrt{2}+1}{\sqrt{2}-1} \cdot Z_0$	$\frac{0.5}{\sqrt{2}} \cdot (1+j) \cdot a_6$
3	0011	0	1	Z_0	Open	$0.5 \cdot j \cdot a_6$
4	0010	$-\frac{1}{\sqrt{2}}$	$\frac{1}{\sqrt{2}}$	$\frac{\sqrt{2}-1}{\sqrt{2}+1} \cdot Z_0$	$\frac{\sqrt{2}+1}{\sqrt{2}-1} \cdot Z_0$	$\frac{0.5}{\sqrt{2}} \cdot (-1+j) \cdot a_6$
5	0110	-1	0	Short	Z_0	$-0.5 \cdot a_6$
6	0111	$-\frac{1}{\sqrt{2}}$	$-\frac{1}{\sqrt{2}}$	$\frac{\sqrt{2}-1}{\sqrt{2}+1} \cdot Z_0$	$\frac{\sqrt{2}-1}{\sqrt{2}+1} \cdot Z_0$	$\frac{0.5}{\sqrt{2}} \cdot (-1-j) \cdot a_6$
7	0101	0	-1	Z_0	Short	$-0.5 \cdot j \cdot a_6$
8	0100	$\frac{1}{\sqrt{2}}$	$-\frac{1}{\sqrt{2}}$	$\frac{\sqrt{2}+1}{\sqrt{2}-1} \cdot Z_0$	$\frac{\sqrt{2}-1}{\sqrt{2}+1} \cdot Z_0$	$\frac{0.5}{\sqrt{2}} \cdot (1-j) \cdot a_6$
9	1000	0.5	0	$3Z_0$	Z_0	$0.25 \cdot a_6$
10	1001	$\frac{1}{2\sqrt{2}}$	$\frac{1}{2\sqrt{2}}$	$\frac{2\sqrt{2}+1}{2\sqrt{2}-1} \cdot Z_0$	$\frac{2\sqrt{2}+1}{2\sqrt{2}-1} \cdot Z_0$	$\frac{0.25}{\sqrt{2}} \cdot (1+j) \cdot a_6$
11	1011	0	0.5	Z_0	$3Z_0$	$0.25 \cdot j \cdot a_6$
12	1010	$-\frac{1}{2\sqrt{2}}$	$\frac{1}{2\sqrt{2}}$	$\frac{2\sqrt{2}-1}{2\sqrt{2}+1} \cdot Z_0$	$\frac{2\sqrt{2}+1}{2\sqrt{2}-1} \cdot Z_0$	$\frac{0.25}{\sqrt{2}} \cdot (-1+j) \cdot a_6$
13	1110	-0.5	0	$1/3 \cdot Z_0$	Z_0	$-0.25 \cdot a_6$
14	1111	$-\frac{1}{2\sqrt{2}}$	$-\frac{1}{2\sqrt{2}}$	$\frac{2\sqrt{2}-1}{2\sqrt{2}+1} \cdot Z_0$	$\frac{2\sqrt{2}-1}{2\sqrt{2}+1} \cdot Z_0$	$\frac{0.25}{\sqrt{2}} \cdot (-1-j) \cdot a_6$
15	1101	0	-0.5	Z_0	$1/3 \cdot Z_0$	$-0.25 \cdot j \cdot a_6$
16	1100	$\frac{1}{2\sqrt{2}}$	$-\frac{1}{2\sqrt{2}}$	$\frac{2\sqrt{2}+1}{2\sqrt{2}-1} \cdot Z_0$	$\frac{2\sqrt{2}-1}{2\sqrt{2}+1} \cdot Z_0$	$\frac{0.25}{\sqrt{2}} \cdot (1-j) \cdot a_6$

24.2.3 Multi-port interferometer for antenna array

An antenna array with adaptive electronically steerable beams will allow mobility, and easy setup compared to a directional one using fixed high gain [15], [16].

The geometrical model of a four-element planar antenna array is presented in Figure 24.4. The patch antennas are spaced by $\lambda_0/2$, where λ_0 is the free-space wavelength. Due to the angle of arrival θ, a difference between two consecutive propagation paths, Δx, will appear.

Consequently, the RF input signals a_i will be phase shifted one versus the other by an angle $\Delta\phi$. As known, this phase shift is directly related to the path difference, expressed by the next equation:

$$\Delta x_i = \lambda_0 \cdot \frac{\Delta\phi_i}{2\pi}, \quad i = 2, 3, 4. \tag{24.25}$$

Using the previous equation, and the geometrical model of Figure 24.4, the angle of arrival can be obtained as follows:

$$\sin\theta = \frac{\Delta x_i}{(i-1)\frac{\lambda_0}{2}} = \frac{\Delta\phi_i}{(i-1)\pi}, \quad i = 2, 3, 4. \tag{24.26}$$

The block diagram of a four element antenna array is shown in Figure 24.5. Its architecture is based on a 4 × 4 Butler matrix using an original topology, adapted to

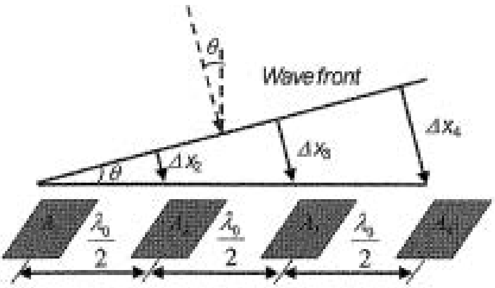

Figure 24.4 Geometrical model of a four-element antenna array.

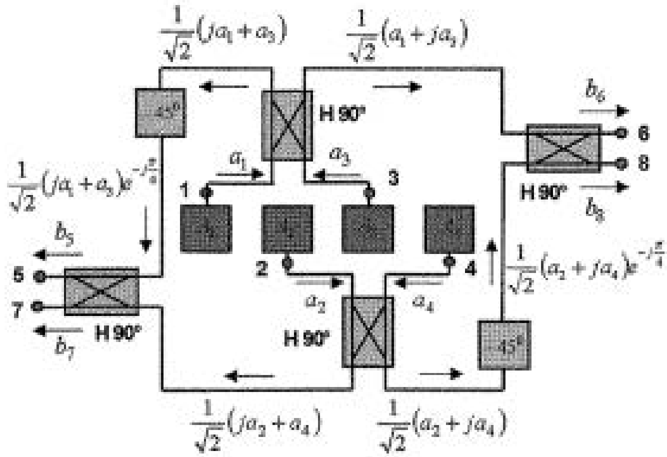

Figure 24.5 Block diagram of four-element antenna array.

millimeter wave frequencies, which avoids any cross line. The four patch antennas are connected to a multi-port circuit, having four inputs and four outputs.

This circuit is composed of four 90° hybrid couplers and two 45° phase shifters, implemented by $\lambda_g/8$ transmission lines. Due to their small dimensions, the patch antennas are integrated on the same substrate.

In order to calculate the multi-port output signals, b_5 to b_8, the pattern factor of a patch antenna in the H-plane is considered [17]:

$$F_H(\theta) = \cos\theta \cdot \frac{\sin\left[\frac{\beta \cdot W}{2} \cdot \sin\theta\right]}{\frac{\beta \cdot W}{2} \cdot \sin\theta}. \tag{24.27}$$

In this equation, β is the free-space propagation constant and $W = \lambda_g/2 = \lambda_0/\left(2\sqrt{\varepsilon_{eff}}\right)$ represents the patch width, selected to obtain a proper radiation resistance R to the input ($R = 50\ \Omega$). Hence, the previous equation becomes:

$$F_H(\theta) = \cos\theta \cdot \frac{\sin\left[\frac{\pi}{2\sqrt{\varepsilon_{eff}}} \cdot \sin\theta\right]}{\frac{\pi}{2\sqrt{\varepsilon_{eff}}} \cdot \sin\theta}. \tag{24.28}$$

According to Equations (24.25) and (24.26), and using the geometrical model of Figure 24.4, the four input signals of the multi-port antenna array, a_1 to a_4, are:

$$a_i = a \cdot e^{-j\Delta\phi_i} \cdot F_H(\theta) = a \cdot e^{-j(i-1)\pi \sin\theta} \cdot F_H(\theta), \quad i = 1, 2, 3, 4. \tag{24.29}$$

Based on the block diagram of Figure 24.5 and the S matrix of the 90° hybrid coupler given by Equation (24.2), the four multi-port output signals b_5 to b_8 can be expressed as follows:

$$b_5 = \frac{1}{2}\left(-a_1 \cdot e^{-j\frac{\pi}{4}} + ja_2 + ja_3 \cdot e^{-j\frac{\pi}{4}} + a_4\right) \tag{24.30}$$

$$b_6 = \frac{1}{2}\left(ja_1 + ja_2 \cdot e^{-j\frac{\pi}{4}} - a_3 + ja_4 \cdot e^{-j\frac{\pi}{4}}\right) \tag{24.31}$$

$$b_7 = \frac{1}{2}\left(ja_1 \cdot e^{-j\frac{\pi}{4}} - a_2 + a_3 \cdot e^{-j\frac{\pi}{4}} + ja_4\right) \tag{24.32}$$

$$b_8 = \frac{1}{2}\left(a_1 + ja_2 \cdot e^{-j\frac{\pi}{4}} + ja_3 - a_4 \cdot e^{-j\frac{\pi}{4}}\right). \tag{24.33}$$

Figure 24.6 shows the computed normalized output signals versus the angle of arrival, using the previous equations. For each output signal, an individual maximum is obtained by shifting θ in a 180° range. The side-lobes are at least 8 dB below the main lobe and the angles of arrival corresponding to the maximum signals are around: −45°, −15°, 15°, and 45°. Therefore, the main lobe of the antenna array can be shifted by 30° multiplies.

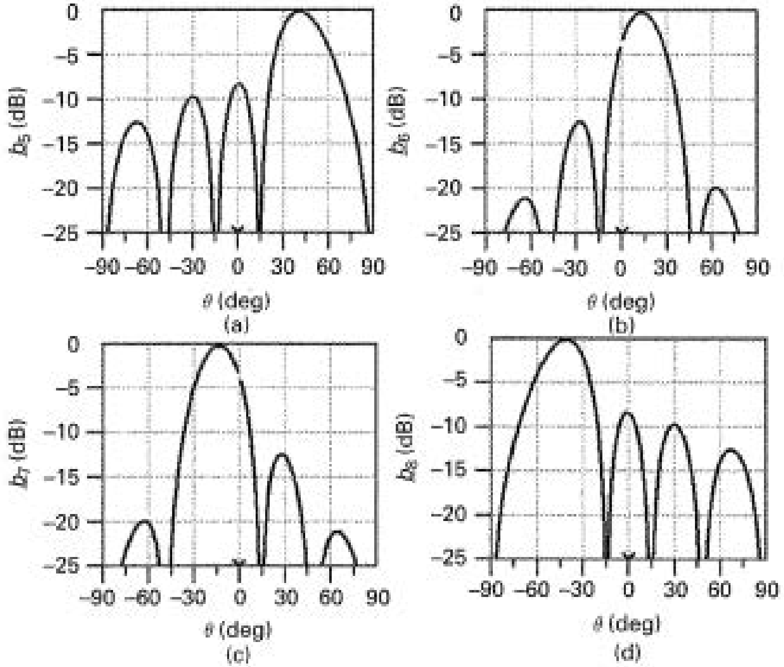

Figure 24.6 Computed normalized output signals versus the angle of arrival.

The antenna array system based on the multi-port interferometer is used in a multiple-input multiple-output (MIMO) architecture as explained in Section 24.4. As seen, this spatial selectivity is achieved by using four fixed received/transmitted beams. A gain improvement, compared with an omnidirectional antenna pattern, is obtained for each angle of arrival. ADS Momentum simulations of this antenna array using the fabrication technology and components presented in the next section show an average directivity of 11 dBi and an average gain of around 8 dB.

Therefore, the proposed beamforming will improve the overall signal-to-noise ratio of the communication link, decreasing the global bit error rate (BER).

24.3 Multi-port V-band practical implementation, modeling, and analysis

In the last decade the multi-port circuit was implemented in various architectures and technologies. The choice of the fabrication technology depends on the operating frequency and application. Miniature Hybrid Microwave Integrated Circuits (MHMIC) [9] and Monolithic Microwave Integrated Circuits (MMIC) [10] technologies were chosen to implement the prototypes of various communication receivers and radar sensors, in homodyne and heterodyne architectures, at Ka and V band frequencies. The Substrate Integrated Waveguide (SIW) [18] and conventional RWG [19] technologies were used at W band frequencies, to support higher power levels requested in radar sensors and phase noise measurement applications.

The typical topology of the circuit was illustrated in Figures 24.1 and 24.3. This multi-port circuit represents the core of the interferometric I/Q demodulator and direct modulator, respectively. Advanced Design System (ADS) Momentum software of Agilent Technologies was used to perform the circuit design in microstrip implementations. A careful design targets the reflection and insertion loss, and the isolation between the RF and reference signals. It is to be noted that, due to its specific architecture, the insertion loss of an ideal multi-port is 6 dB. Therefore, the phase result of the transmission signals is critical to obtain the desired combination of input signals through the four outputs. The isolation between the millimeter wave inputs is also a very important criterion of the communication systems. Moreover, in order to reduce the DC offset caused by the multiple reflections at the outputs, the return losses at all ports, at the operating frequency, must be excellent.

A V-band multi-port circuit was designed in MHMIC technology using a ceramic substrate, having a 9.9 relative permittivity and 125 μm thickness. The circuit topology is based on the schematic presented in Figures 24.1 and 24.3, as seen in the microphotographs of Figure 24.7. In order to avoid reflections at all unused ports of the multi-port circuit during two port measurements, integrated 50 Ω loads are connected to the open circuit quarter-wave transmission lines (representing virtual RF short-circuits in the operating band). The diameter of the Wilkinson power divider and that of the hybrid coupler are around 1 mm and 0.7 mm, respectively. The 50 Ω line width is practically equal to the substrate thickness.

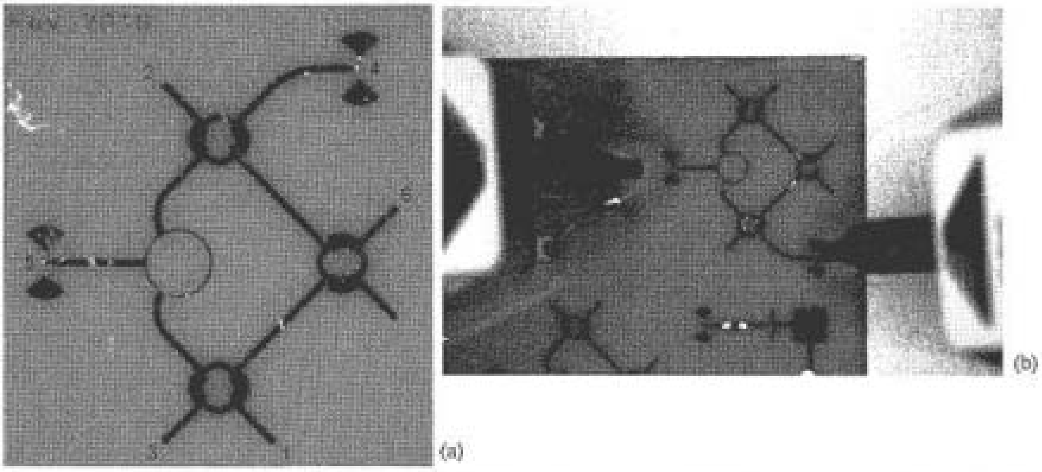

Figure 24.7 Microphotograph of the V-band MHMIC multi-port prepared for S_{52} measurement (a), and a detail of its on-wafer measurements (b).

On-wafer multi-port S parameter measurements are performed using a millimeter wave Precision Network Analyzer (PNA) of Agilent Technologies and a Cascade Microtech probe station equipped with ground signal ground (GSG) 150 μm pico-probes.

Figure 24.8 presents typical S parameter measurement results of this multi-port circuit, over 4 GHz frequency band, between 60 and 64 GHz. The lower measurement limit of 60 GHz is imposed by the PNA frequency range of 60–90 GHz. However, these results can be easily extrapolated over 57–60 GHz band using the acquired measurements, combined with the multi-port ADS Momentum simulations. As seen, good performances in term of return loss at all ports and RF input ports' isolation, are obtained. In addition, the power split between the RF reference input and the four outputs is quasi-constant over the band, and close to the theoretical value of −6 dB, as presented in Figure 24.8(c). It is to be noted that comparable measurement results have been obtained for the other RF input port. As seen in Figure 24.8(d), the use of the V-band hybrid couplers engenders a quasi-constant 90° phase difference over a wide band, suitable for a high-performance quadrature down-converter or direct modulator.

In order to perform advanced system simulations, a multi-port model based on the block diagrams of Figures 24.1 and 24.3 is implemented in ADS, using full S-parameter measurements of the Wilkinson power divider and 90° hybrid coupler. This model has been preferred instead of one based on multi-port full S-parameter measurements, which requires the fabrication of 15 different circuits to cover all two-port measurements. The multi-port model has been validated through comparison with its available measurements, such as presented in Figure 24.8. A very good agreement is obtained between the model simulation and the measurement results.

To demonstrate that the multi-port is a four "q_i points" circuit [2] having all points spaced by 90°, a harmonic balance simulation is performed at 61 GHz. Both RF input signals have the same frequency (homodyne case). The phase difference between the

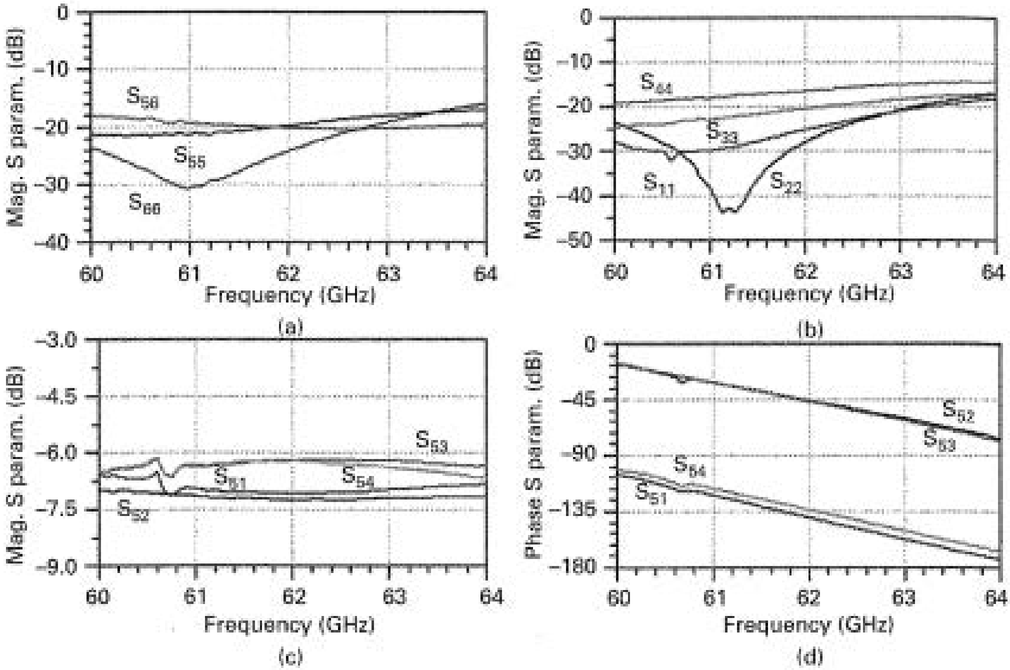

(a) (b) (c) (d)

Figure 24.8 Measured typical S-parameters of the V-band multi-port.

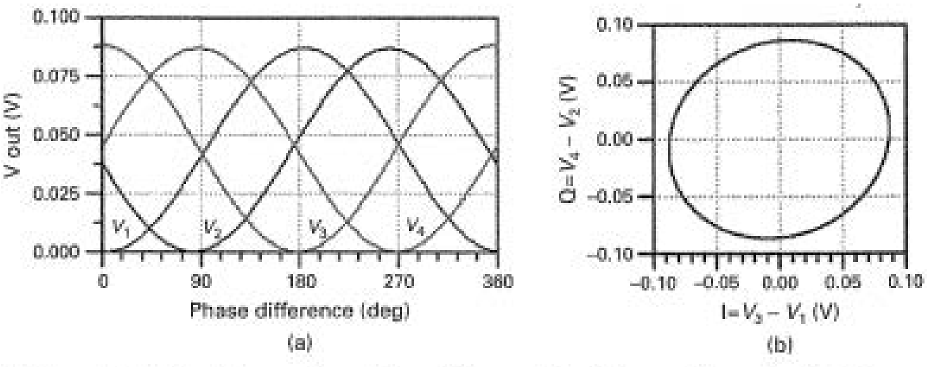

(a) (b)

Figure 24.9 Multi-port detected voltages vs. input phase difference (a) and the quadrature signals (b).

millimeter wave inputs is swept in a 360° range and the RF input signal power is set to 0 dBm. Power detectors are connected at the four outputs.

The multi-port detected output voltages versus the RF input signals' phase difference are presented in Figure 24.9(a). As seen, the output voltage minimum values are shifted by 90° multiples, as requested for this architecture. In addition, the output voltages at the pairs of ports 1 and 3, and 2 and 4, respectively, are phase opposites. Therefore, I/Q output signals can be obtained using a differential approach, as sustained by Equations (24.12) and (24.13), and illustrated in Figure 24.9(b). As seen, the shape is quasi-circular and practically centered in the origin (low DC offset), proving very good capabilities of the proposed multi-port to perform quadrature operation.

In order to demonstrate the multi-port demodulation capabilities, an ADS envelope simulation is performed in homodyne architecture, using a schematic based on Figure 24.1. Various modulation schemes have been implemented and analyzed. Let's see some results. In the case of Amplitude Modulation (AM), the Γ vector, defined by Equation (24.16), has a linear variation, while maintaining a constant phase. In the case of frequency modulation (FM), the constant magnitude of Γ vector turns on a circle, and rotates clockwise or anticlockwise with the instantaneous frequency difference between the input ports.

As known, in a digital modulation, each combination of magnitude and phase is called a *symbol* and represents a digital bit stream. QAM technique is used to analyze error vectors in the down-conversion process.

In the ADS envelope simulation, the LO power is set at as low as −25 dBm, and the low-noise amplifier (LNA) input signal at −45 dBm. The LNA model is based on the data sheet of the Hittite HMC-ALH382, high gain GaAs HEMT LNA (57–65 GHz, 21 dB of gain, NF = 3.8 dB). The millimeter wave power detector models are based on the Spice model of the zero-bias Schottky diode, model HSCH-9161, of Agilent Technologies. Matching networks are used to improve the return loss over the 60 GHz band. Each differential amplifier module uses two dual wide-band OPA 2658 low-power current feedback operational amplifiers (Burr-Brown). Its model is implemented in ADS based on the manufacturer's data sheet. The total gain of the module is 20 dB, and is validated by measurements on a test bench.

Figure 24.10(a) shows dual-ring 16-Star QAM demodulation results. The modulation scheme looks like a dual 8-PSK having a radius ratio of 2. In addition, Figure 24.10(b) shows the results of the well-known Square 16-QAM demodulation.

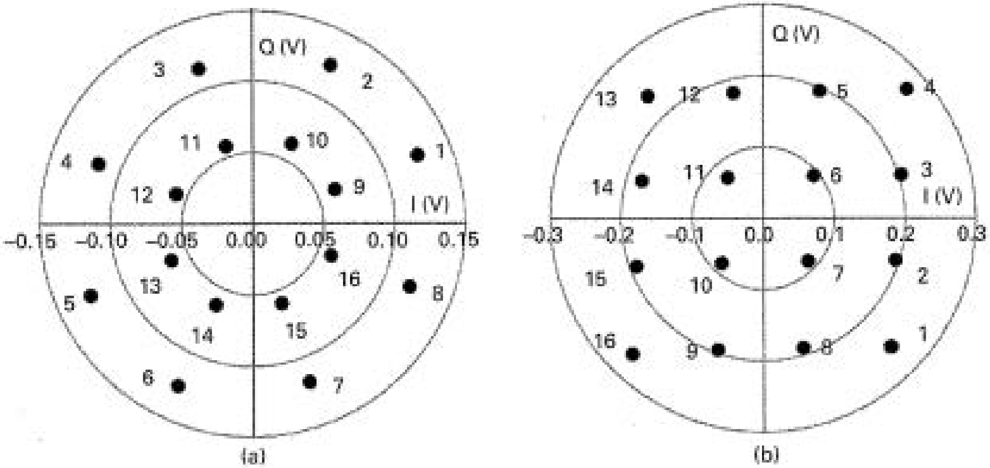

(a) (b)

Figure 24.10 Dual-ring 16-Star QAM and Square 16-QAM demodulation results.

The Γ vector mapping in the baseband complex plane is presented for each of the 16 symbols. The resulting error vector represents the difference between the actual demodulated and the ideal symbol vectors. To remove the dependence on system gain distribution, related magnitude and phase errors are calculated for each symbol [20]. For both demodulation schemes, these errors are less than 5 percent, showing good demodulation performances without using any calibration techniques.

24.4 Proposed transceiver architectures

According to FCC definition, the transmission bandwidth of UWB signals should be greater than 500 MHz or larger than 20 percent of the central frequency. This open definition does not specify any air interface or modulation for UWB. In the early stages, time-domain impulse radio (IR) dominated UWB technology and still plays a crucial role today. However, driven by the standardization activities, conventional modulation schemes, such as Single Carrier (SC), Frequency Division Multiplexing (FDM), or Orthogonal Frequency Division Multiplexing (OFDM), have also appeared [21].

As known, the OFDM technique partitions a UWB channel in a group of non-selective narrowband channels (using a simple modulation technique such as QPSK), which makes it robust against large delay spreads, by preserving orthogonality in the frequency domain. For multi-carrier systems, two approaches can be used: (i) a high number of carriers (16, 32, 64, or 128) with a corresponding relatively low bit-rate/carrier, or (ii) a small number of carriers (2, 4, or 8) with a corresponding higher bit-rate/carrier. However, at 60 GHz, phase noise and carrier offset will degrade the multi-carrier system performances. Due to the complexity of these architectures, in the authors' opinion, only the second approach is suitable for low-cost 60 GHz UWB WLANs.

The available bandwidth, together with the efficient reuse of spectrum (due to the strong signal attenuation at 60 GHz) makes flexibility, simplicity, and cost, the most critical points of these communication systems. It was demonstrated that the transmissions using SC advanced modulation techniques and directive antennas can achieve comparable performances with OFDM, for a 60 GHz indoor channel [21]. These modulations, such as M-ary QAM and M-ary PSK, will considerably increase the spectral efficiency.

The simulation results of a 60 GHz high-speed multi-port heterodyne receiver have been published in [12]. A bit-rate up to 400 Mb/s has been achieved using a 16 QAM modulation and an IF of 900 MHz. The proposed architecture enables the design of compact and low-cost wireless millimeter wave communication receivers for future high-speed WLANs, according to the IEEE 802.15.3c standard. However, to cope with the Gb/s bit-rates, the millimeter wave circuits' bandwidth must be increased to a few GHz, and the IF must be at least 2.45 GHz.

Due to the high free-space loss at the carrier frequency, transmission on ranges up to 10 meters can be expected. The Friis path loss equation [22] shows that, for equal antenna gains, path loss increases with the square of the carrier frequency. Therefore, 60 GHz communications have an additional 22 dB of path loss when compared to an equivalent

5 GHz system. However, antenna dimensions are inversely proportional to carrier frequency. Therefore, more antennas can be placed within a fixed area and the resulting antenna array will improve the overall antenna gain. The directive pattern of a beam forming antenna array improves the channel multipath profile by limiting the spatial extent of the transmitting and receiving antenna patterns to the dominant transmission path. This aspect opens up new opportunities for wireless system design. The use of smart antennas will also improve the link budget and will reduce the transmitter power [23].

A consequence of the confinement to smaller cells is that the channel dispersion is smaller than the values encountered at lower frequencies, because the echo paths are shorter on average. However, movements of the portable stations, as well as the movement of objects in an environment, cause Doppler effects, relatively severe at 60 GHz, because they are proportional to the carrier frequency. For example, if a person moves at a walking speed of 1.5 m/s, the Doppler spread result is 1200 Hz.

In the case of a single carrier, the use of directive antenna arrays based on multi-ports, a heterodyne multi-port I/Q down-converter, and a multi-port modulator, is considered very promising for indoor low-cost UWB communications.

Figure 24.11 shows a simplified block diagram of a single-carrier millimeter wave multi-port direct conversion transceiver. A MIMO architecture using two phased arrays based on Butler matrices is proposed. This solution appears optimal because a few discrete beam directions are generally sufficient for indoor WLANs. A 20 GHz microwave oscillator and a frequency multiplier generate the 60 GHz signal. The digital signal

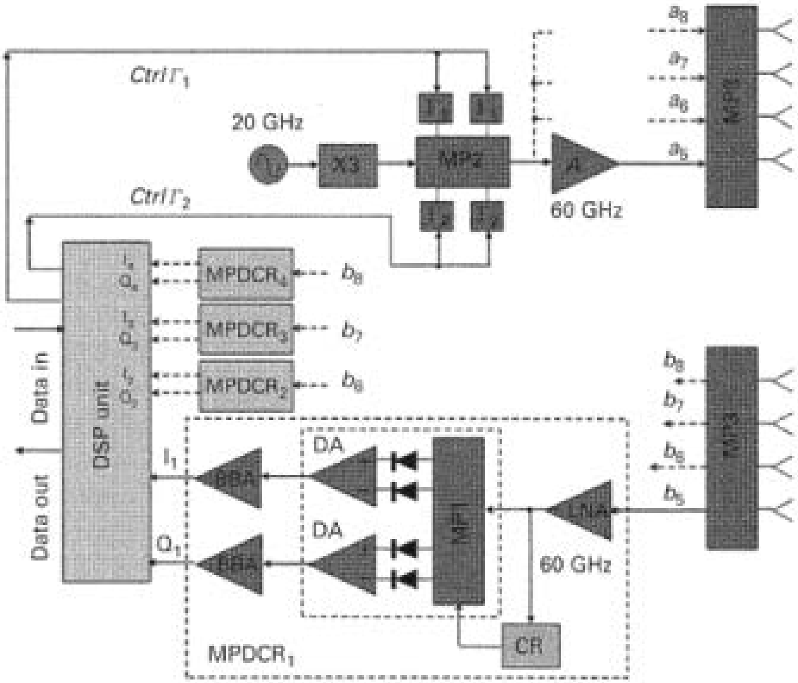

Figure 24.11 Simplified block diagram of a single carrier multi-port direct conversion transceiver.

processing (DSP) unit modulates the carrier using a multi-port direct modulator MP2. According to the 60 GHz related standard, the amplifier's maximum output power is +10 dBm.

Identical multi-port antenna arrays MP3 are used for transmitter and receiver units. Four multi-port direct conversion receivers (MP DCR_i) are connected directly to the receiver's multi-port antenna array. Each receiver is composed of an LNA, a carrier recovery circuit (CR), a multi-port down-converter (MP1, power detectors, and differential amplifiers (DA)), and two baseband amplifiers (BBA). The DSP unit will dynamically select the strongest quadrature received signal (the optimum direction of arrival) and will activate the corresponding millimeter wave amplifier to feed the transmitter's multi-port antenna array MP3.

Analog-to-digital (A/D) converters are used at the DSP input. It is important to underline that the received baseband signal data rate (frequency) is significantly lower than the frequency of the millimeter wave signal. In addition, the signal level is significantly increased due to the overall gain of the millimeter wave receivers. That's why the A/D converters are not connected directly to the multi-port antenna array output, and, consequently, the processing of the millimeter wave signal cannot be moved to the digital side. We note that the baseband analog signal levels are tens of millivolts and their frequency is related to data rate (hundreds of MHz). The baseband signal processing is the optimum and unique solution with today's technology.

The access to the in-phase (I) and quadrature (Q) signals will enable significant additional capabilities, increasing the phase measurement accuracy and offering a straightforward correspondence between the baseband phasor rotation frequency and the Doppler shift, if the same oscillator is used in the receiver part. The carrier recovery circuit is used as reference signal and will compensate the Doppler shift in a hardware approach.

Figure 24.12 shows the proposed heterodyne architecture of a multi-port transceiver. Due to the increased gain of the receiver, omni-directional antennas can also be used. An additional millimeter wave oscillator is introduced in the receiver part, due to the non-zero IF. The Doppler effects and the inherent frequency shift between millimeter wave oscillators are compensated using a phase-locked loop (PLL) circuit, operating at IF. The second down-conversion can easily use conventional means, due to the relatively low operating frequency. To cope with data-rates of 500 Mb/s, the IF of the heterodyne receiver is chosen at 900 MHz. If the data-rate is increased to 1 Gb/s, the IF can be chosen at 2.45 GHz.

As seen in the previous section (Figure 24.10), in the case of a perfect synchronism, the demodulation errors, without any multi-port calibration, are less than 5 percent. However, a digital compensation technique is implemented in the DSP unit. For example, based on the minimum "distance" between each demodulated quadrature symbol and the ideal map of symbols (corresponding to each modulation scheme), the inherent mismatch in demodulated symbol mapping is compensated. Furthermore, the data output is generated according to each specific modulation chart (e.g. see Tables 24.1 to 24.4 for QPSK, 8PSK, Square 16-QAM, and 16-Star QAM) using digital-to-analog (D/A) converters.

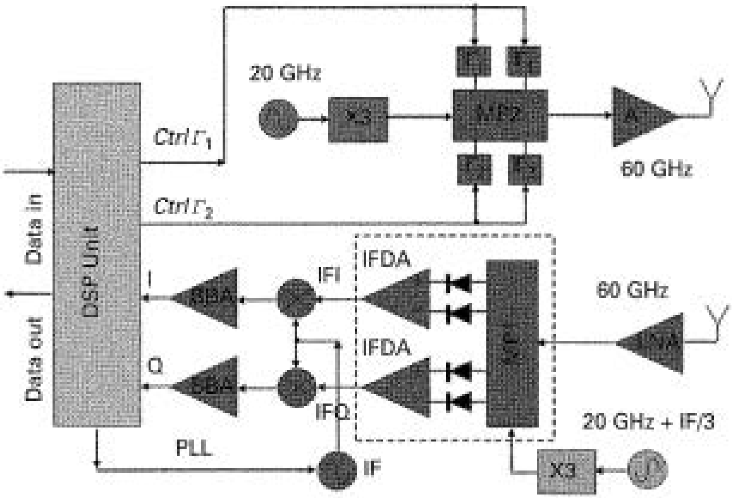

Figure 24.12 Simplified block diagram of a single carrier multi-port heterodyne transceiver.

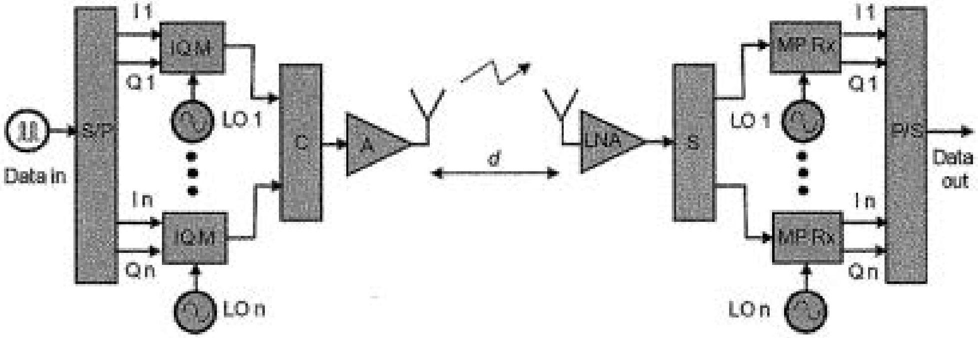

Figure 24.13 Simplified block diagram of an FDM wireless link.

The wireless link is implemented using a FDM system based on UWB millimeter wave multi-port circuits, as seen in Figure 24.13. The channel plan is related to the requested bit-rate, modulation technique, and available band. A serial to parallel converter (S/P) with $2n$ parallel outputs, n millimeter wave LO, n quadrature modulators, and n way millimeter wave combiner (C), are used to generate the FDM signal. This signal is amplified (A) and transmitted through an antenna. After being amplified by the LNA, the received signal is split (S) and coherently demodulated, using n multi-port receivers (MP Rx). Finally, a parallel-to-serial data converter (P/S) generates the output data stream. Due to the UWB characteristics, identical multi-port circuits can be used for both direct modulation and demodulation.

Direct Sequence (DS) UWB is often referred to as impulse, baseband, or zero carrier technique. It operates by sending Gaussian low-power shaped pulses, coherently received by the receiver. Considering that the system operates using pulses, the transmission spreads out, typically, many hundreds of MHz or even several GHz, over a wide bandwidth. To enable data to be carried, DS UWB transmissions can be modulated in multiple ways. For example, Pulse Position Modulation (PPM) encodes the information by modifying the time interval and, hence, the position of the pulses; and Binary Phase Shift Keying (BPSK) reverses the phase of the pulse to modulate the data to be transmitted. Therefore, in order to use a larger bandwidth with reduced power consumption, a new method based on the transposition of Impulse Radio Ultra Wideband (IR UWB) signals at 60 GHz-band can also be taken into account [24]–[26].

As a low-cost 60 GHz IR UWB proposal, presented in Figure 24.14, the transmitter part can be implemented using an oscillator, a millimeter wave switch, and an amplifier. A pulse generator (first PG) generates sub-nanoseconds pulses (for example pulse width around 350 ps, in order to reach 3 GHz bandwidth). The 60 GHz carrier will be digitally pulse position modulated (PPM) using a millimeter wave switch. After amplification, Gaussian pulses are emitted over several GHz of bandwidth, centered into the 60 GHz band. In order to implement the receiver, either a mixer or a detector can be used. If a mixer is used, a millimeter wave LO is needed. The mixer can be implemented using the low-cost, low-power consumption multi-port down-converter. The oscillator is not required when a topology with a detector is chosen, as presented in the figure. Therefore, the receiver is composed of three main modules: a low-noise amplifier, a 60 GHz detector, and a correlator. A pulse generator (second PG) is used to control the sample and hold (S/H) circuit. The main advantage of this architecture is that no phase information is needed, and thus, no sophisticated coherent stable sources or carrier recovery circuits are involved. It is to be noted that the pulses can also be modulated using the BPSK, with minimal architectural changes in both transmitter and receiver modules. In order to transmit data information, instead of modifying the position of pulses as for PPM, the phase of sub-nanosecond pulses will be reversed at the transmitter. The receiver must be able to observe these 180° phase changes; therefore, a multi-port based phase-detector can be successfully used. It is to be noted that, as usual in block diagrams, the DSP include required A/D and D/A converters.

The proposed architectures enable the design of compact and low-cost wireless millimeter wave transceivers for future UWB wireless communication systems.

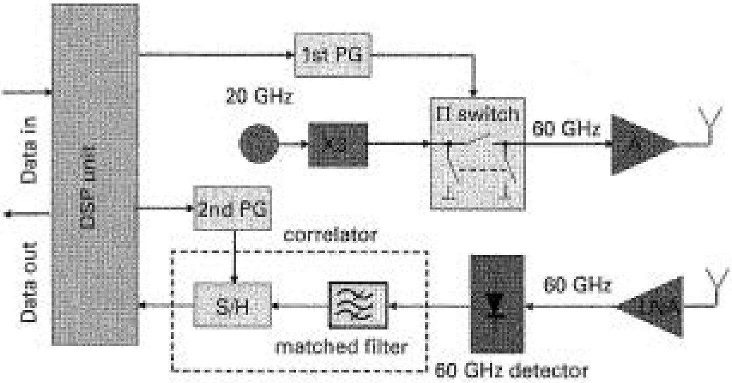

Figure 24.14 Simplified block diagram of an impulse-radio transceiver.

24.5 Advanced system simulations

Advanced Design System software of Agilent Technologies is used to validate multi-port transceiver architectures. Both single-carrier and multi-carrier approaches are discussed in this chapter. The simulation block diagrams are drawn according to the schematics presented in the previous section.

In the first instance, a single-carrier architecture is analyzed. Figure 24.15 shows the spectrum of the QPSK signal used in the simulations. The symbol rate per carrier (SRC) is selected at 500 MS/s, corresponding to a data rate of 1 Gb/s. The main lobe is centered, in this case, at 62 GHz.

According to well known Friis equation [22], the free space LOS attenuation is equal to 88 dB for $d = 10$ m range. In this system analysis, the antenna gains are set at 10 dBi. As in the multi-port analysis section, the LNA gain and the noise figure (NF) are 21 dB and 3.8 dB, respectively, a common value for today's 60 GHz integrated amplifiers. To obtain data output squared waves, and, consequently, perfect demodulated constellations, limiters are used in the baseband (BB) stage of the receiver. We note that this approach can be used only for BPSK or QPSK modulation schemes.

As seen in Figure 24.16(a), (b), and (c), for a pseudo-random bit sequence of 200 ns length, the output demodulated I signals have the same bit sequence as that transmitted. Equivalent results are obtained for Q signals.

Figure 24.17 shows the BER variation versus the Eb/No ratio, where Eb is the average energy of a modulated bit, and No is the noise power spectral density. Obviously, this six-port receiver architecture using a single-carrier scheme has excellent BER performances, close to the theoretical one (dotted line). This result proves its high potential to be used in wireless HD (High Definition) communications.

A second analysis based on four carrier FDM architecture to validate the use of 60 GHz UWB multi-ports in multi-carrier systems is performed. A 4 Gb/s data-link is analyzed using the QPSK modulation of equidistant carriers at 60, 61, 62, and 63 GHz, respectively, and an SRC of 500 MS/s. The data-rate can be further increased, if needed, using

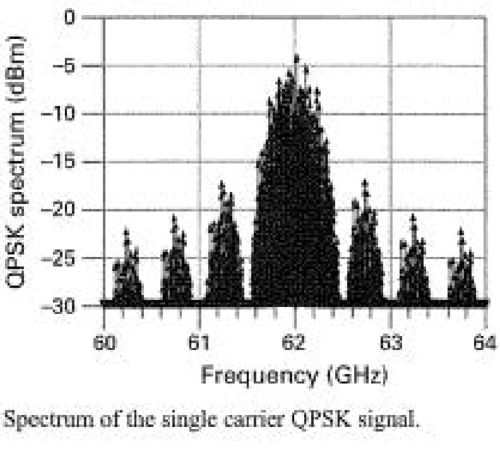

Figure 24.15 Spectrum of the single carrier QPSK signal.

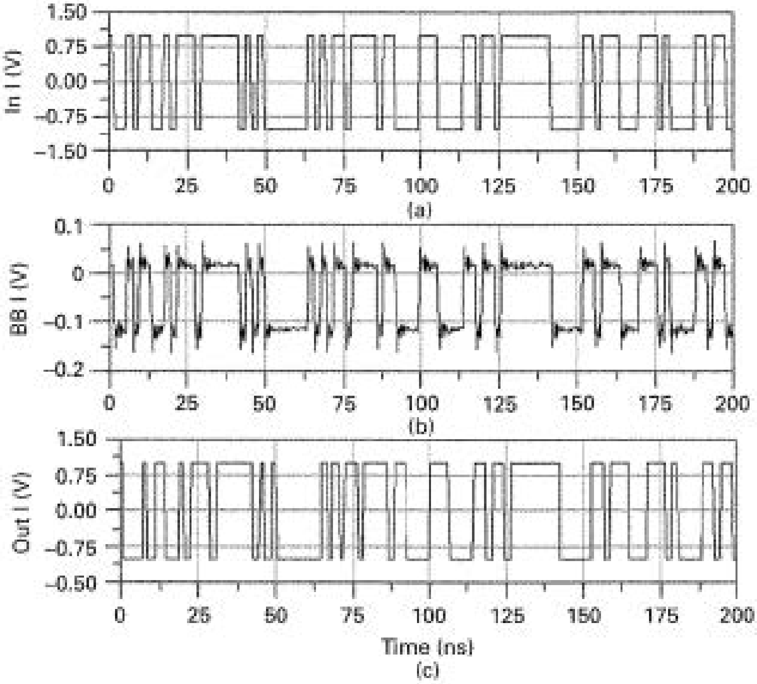

Figure 24.16 Demodulation results of 1 Gb/s QPSK pseudo-random signal: (a) transmitted, (b) received baseband signal, after differential amplifiers, (c) demodulated, at the limiter output.

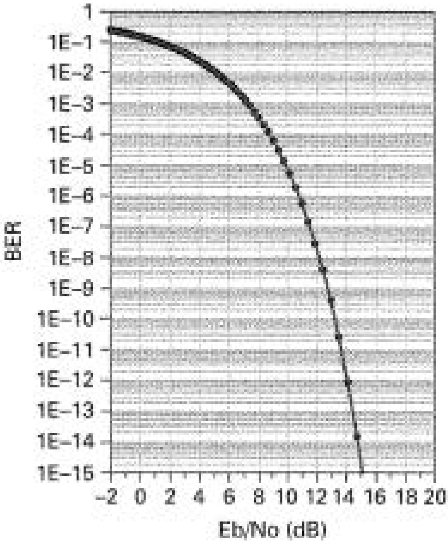

Figure 24.17 BER results for 1 Gb/s QPSK signal.

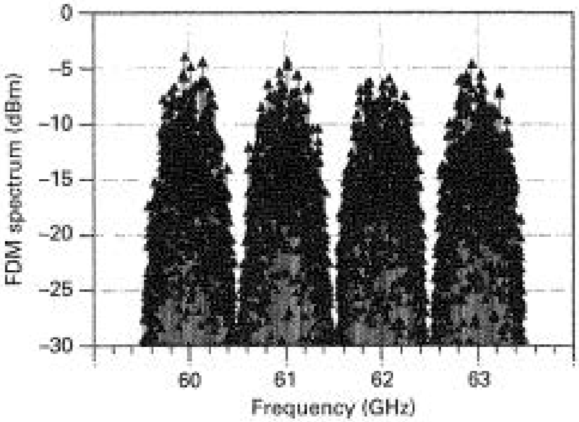

Figure 24.18 Spectrum of the four carrier FDM signal.

the whole spectrum of 7 GHz (57–64 GHz) or the OFDM technique. It is to be noted that our multi-port model is implemented starting from 60 GHz, due to the available instrument's measurement capabilities (60–90 GHz).

According to the schematic presented in Figure 24.13, an ADS envelope simulation is performed. In order to cover the whole FDM spectrum of 4 GHz, a simulation step of 1/(14·SRC) is considered. The FDM spectrum, at the transmitting antenna input, is shown in Figure 24.18. As requested for the FDM, the sub-channel spectrums are not overlapped.

In order to evaluate the wireless link quality, a BER analysis is performed for each sub-channel. As seen in Figure 24.19, BER results are presented as a function of Eb/No ratio. All sub-channels have quasi similar BER results, demonstrating once again the UWB performances of the multi-port.

Furthermore, because the transmitted symbols are uncorrelated, the global BER can be estimated using an analytical approach. The BER average is considered as the sum of the BER related to each sub-channel [27] and is obtained using the following equation:

$$P_{Sys} = \frac{1}{N \cdot \log_2 M} \cdot \sum_{i=1}^{N} (BER)_i. \tag{24.34}$$

In the previous equation, P_{Sys} is the global error probability (or BER) of the proposed system, N is the number of carriers which are used, M is related to the modulation levels or number of bits per symbol (for QPSK, M = 2), and $(BER)_i$ is the BER of each sub-carrier.

Figure 24.20 shows the BER average curve of the system at 4 Gb/s, as well as the BER corresponding to the single-carrier communication system at 1 Gb/s. It is obvious that, by using the multi-carrier modulation techniques, for a BER = 10^{-9}, Eb/No should be incremented by about 2 dB, which is not considered a critical disadvantage. In the meanwhile, a noticeable high data rate of 4 Gb/s is attained.

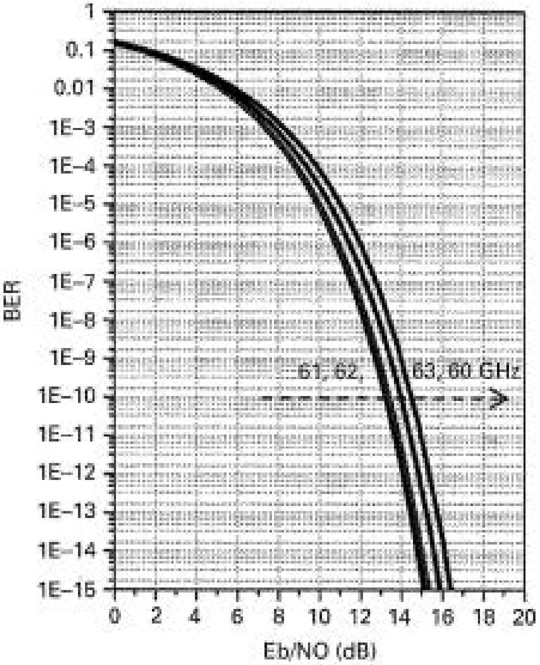

Figure 24.19 BER results for individual FDM sub-channels.

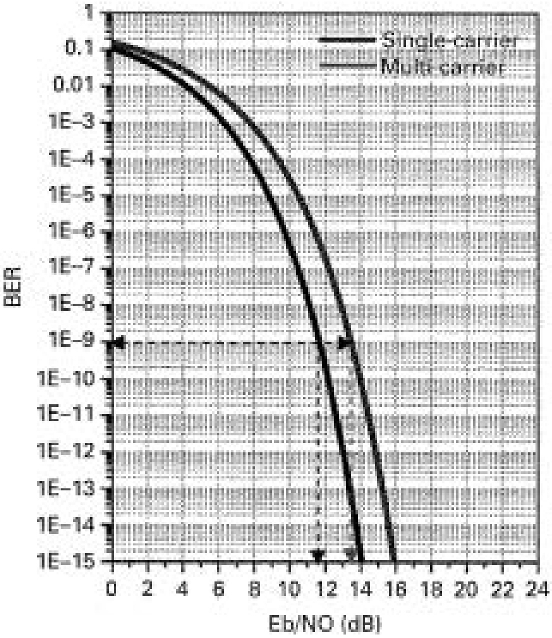

Figure 24.20 BER calculation for FDM system.

24.6 Conclusion

The chapter illustrates the interferometric concept proposed for V-band UWB multi-gigabit/second communication systems. As presented, multi-port circuits can successfully be used in quadrature down-converters, antenna arrays, and direct modulation of millimeter wave signals. An important advantage in using multi-ports is the reduced LO power requested for down-conversion. This is particularly true in millimeter wave applications where the received RF signal is considerably low, reducing both the cost of LO and the leakage between LO and the RF input. Millimeter wave antenna arrays and direct modulators can also take advantage of this interferometric approach with compact and reliable designs.

Single- and multi-carrier architectures are analyzed using advanced system simulations. Despite amplitude and phase imbalances, due to inherent design and fabrication errors of the circuits, the UWB multi-port systems provide excellent demodulation results over the 60 GHz band. For example, the proposed wireless system is able to transmit 4 Gb/s data-rate up to 10 m range, providing a BER of 10^{-9}, as requested for an uncoded HDTV wireless transmission in home or office environments.

Future works will benefit from rapid advances in MMIC technologies to design interferometric millimeter wave transceivers for advanced communication, radar and imaging systems.

References

[1] S. B. Cohn, N. P. Weinhouse, An Automatic Microwave Phase Measurement System. *Microwave Journal*, **7**:2 (1964), 49–56.

[2] G. F. Engen, C. A. Hoer, Application of an Arbitrary 6-Port Junction to Power-Measurement Problems. *IEEE Transactions on Instrumentation and Measurement*, **21**:11 (1972), 470–474.

[3] G. F. Engen, The Six-Port Reflectometer. An Alternative Network Analyzer. *IEEE Transactions on Microwave Theory and Techniques*, **25**:12 (1977), 1075–1077.

[4] G. F. Engen, An Improved Circuit for Implementing the Six-Port Technique of Microwave Measurements. *IEEE Transactions on Microwave Theory and Techniques*, **25**:12 (1977), 1080–1083.

[5] E. Moldovan, R. G. Bosisio, Wu Ke, S. O. Tatu, *Microwave and Millimeter Wave Technologies*, ch. 19 Multi-Port Technology and Applications, 363–388, 1st edn. (Vienna: In-Tech, 2010).

[6] J. Li, Ke Wu, R. G. Bosisio, A Collision Avoidance Radar Using Six-Port Phase/Frequency Discriminator (SPFD). *Proceedings of IEEE Microwave Theory and Techniques Symposium*, (1994), 1553–1556.

[7] J. Li, R. G. Bosisio, Ke Wu, Computer and Measurement Simulation of a New Digital Receiver Operating Directly at Millimeter-Wave Frequencies. *IEEE Transactions on Microwave Theory and Techniques*, **43**:12 (1995), 2766–2772.

[8] J. Li, R. G. Bosisio, Ke Wu, Dual-Ton Calibration of Six-Port Junction and Its Application to the Six-Port Direct Digital Millimetric Receiver. *IEEE Transactions on Microwave Theory and Techniques*, **44**:1 (1996), 93–99.

[9] S. O. Tatu, E. Moldovan, Ke Wu, R. G. Bosisio, A New Direct Millimeter Wave Six-Port Receiver. *IEEE Transactions on Microwave Theory and Techniques*, **49**:12 (2001), 2517–2522.

[10] S. O. Tatu, E. Moldovan, G. Brehm, Ke Wu, R. G. Bosisio, Ka-Band Direct Digital Receiver. *IEEE Transactions on Microwave Theory and Techniques*, **50**:11 (2002), 2436–2442.

[11] S. O. Tatu, E. Moldovan, Ke Wu, R. G. Bosisio, T. Denidni, Ka-Band Analog Front-End for Software-Defined Direct Conversion Receiver. *IEEE Transactions on Microwave Theory and Techniques*, **53**:9 (2005), 2678–2776.

[12] S.O. Tatu, E. Moldovan, V-Band Multiport Heterodyne Receiver for High-Speed Communication Systems. *EURASIP Journal on Wireless Communications and Networking*, Article ID 34358 (2007).

[13] D. Hammou, N. Khaddaj Mallat, E. Moldovan, *et al.*, V-band Six-Port Down-conversion Techniques, *International Symposium on Signals, Systems, and Electronics, ISSSE*, conference CD, IEEE catalog Number 07EX1869C, (2007), 379–382.

[14] R. G. Bosisio, Y. Y. Zhao, X. Y. Xu, *et al.*, New-Wave Radio, *IEEE Microwave Magazine*, **2** (2008), 89–100.

[15] K. Leong, T. Itoh, Advanced and Intelligent RF Front-End Technology, *Wireless Communication Technology*, Conference Proceedings, (2003), 190–193.

[16] E. Moldovan, S.O. Tatu, S. Affes, A 60 GHz Multi-Port Front-End Architecture with Integrated Phased Antenna Array, *Microwave and Optical Technology Letters*, **50**:5 (2008), 1371–1376.

[17] W.L. Stutzman, G.A. Thiele, *Antenna Theory and Design*, 2nd edn. (New York: Artech House, 1997).

[18] E. Moldovan, R.G. Bosisio, Ke Wu, W-Band Multiport Substrate-Integrated Waveguide Circuits. *IEEE Transactions on Microwave Theory and Techniques*, **54**:2 (2006), 625–632.

[19] S.O. Tatu, E. Moldovan, S. Affes, *et al.*, Six-Port Interferometric Technique for Accurate W-band Phase Noise Measurements. *IEEE Transactions on Microwave Theory and Techniques*, **56**:6, (2008), 1372–1379.

[20] S.O. Tatu, R.I. Cojocaru, E. Moldovan, Interferometric Quadrature Down-Converter for 77 GHz Automotive Radar: Modeling and Analysis, *7th European Radar Conference*, (2010), 125–128.

[21] C. Park, T.S. Rappaport, Short-range Wireless Communications for Next-generation Networks: UWB 60 GHz millimeter-wave WPAN, and ZigBee. *IEEE Wireless Communications*, **14**: 4 (2007), 70–78.

[22] D.M. Pozar, *Microwave and RF Design of Wireless Systems*, (New York: John Wiley and Sons, 2001).

[23] S.O. Tatu, E. Moldovan, S. Affes, Low-cost Transceiver Architectures for 60 GHz Ultra Wideband WLANs. *International Journal of Digital Media Broadcasting*, Article ID 382695 (2009).

[24] M. Devulder, N. Deparis, I. Telliez, 60 GHz UWB Transmitter for use in WLAN Communications. *International Symposium on Signals, Systems, and Electronics, ISSSE 2007*, Conference Proceedings, (2007), 371–374.

[25] N. Deparis, A. Boé, C. Loyez, N. Rolland, P.A. Rolland, UWB-IR Transceivers for Millimeter Wave WLAN. *32nd IEEE Industrial Electronics Conference* (2006), 4785–4789.

[26] N. Deparis, A. Bendjabballah, A. Boe, *et al.*, Transposition of Baseband UWB Signal at 60 GHz for High Data Rate Indoor WLAN. *IEEE Microwave and Wireless Components Letters*, **15**: 10 (2005), 609–611.

[27] J. G. Proakis, *Digital Communications*, 3rd edn. (Boston: McGraw-Hill, 1995).

Digital Front-End

in Wireless Communications and Broadcasting

Covering everything from signal processing algorithms to integrated circuit design, this complete guide to digital front-end is invaluable for professional engineers and researchers in the fields of signal processing, wireless communication, and circuit design. Showing how theory is translated into practical technology, it covers all the relevant standards and gives readers the ideal design methodology to manage a rapidly increasing range of applications. Step-by-step information for designing practical systems is provided, with a systematic presentation of theory, principles, algorithms, standards, and implementation. Design trade-offs are also included, as are practical implementation examples from real-world systems. A broad range of topics is covered, including digital pre-distortion (DPD), digital up-conversion (DUC), digital down-conversion (DDC), and DC-offset calibration. Other important areas discussed are peak-to-average power ratio (PAPR) reduction, crest factor reduction (CFR), pulse-shaping, image rejection, digital mixing, delay/gain/imbalance compensation, error correction, noise-shaping, numerically controlled oscillator (NCO), and various diversity methods.

Fa-Long Luo, Ph.D., is Chief Scientist of two leading international companies on software defined radio and wireless multimedia with headquarters in Silicon Valley, California. He has 27 years of research and industrial experience in multimedia, communication, and broadcasting with real-time implementation, applications, and standardizations with worldwide recognition. He has authored two books, more than 100 technical papers, and 18 patents in these and closely related fields.

Cover illustration: original image
© iStockphoto.com / Zane Waldman.

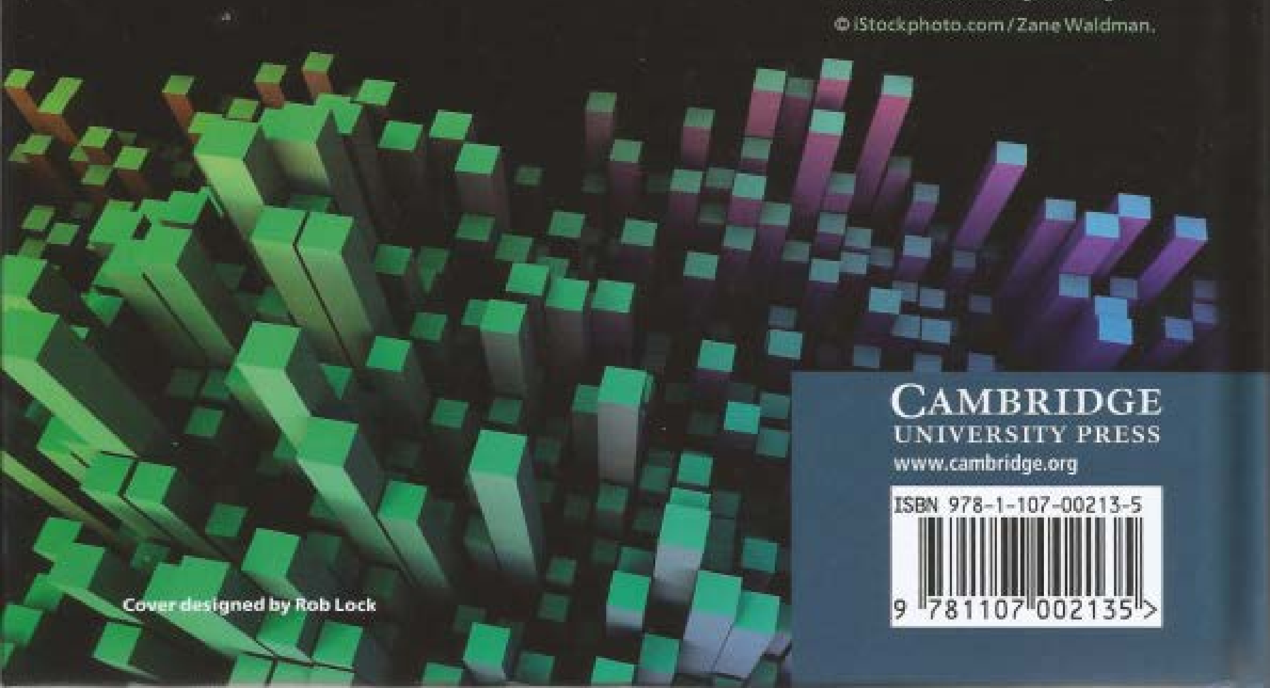

Cover designed by Rob Lock

CAMBRIDGE
UNIVERSITY PRESS
www.cambridge.org

ISBN 978-1-107-00213-5

9 781107 002135